



# Synthesis and Application of Fe-Doped $\text{WO}_3$ Nanoparticles for Photocatalytic Degradation of Methylparaben Using Visible-Light Radiation and $\text{H}_2\text{O}_2$

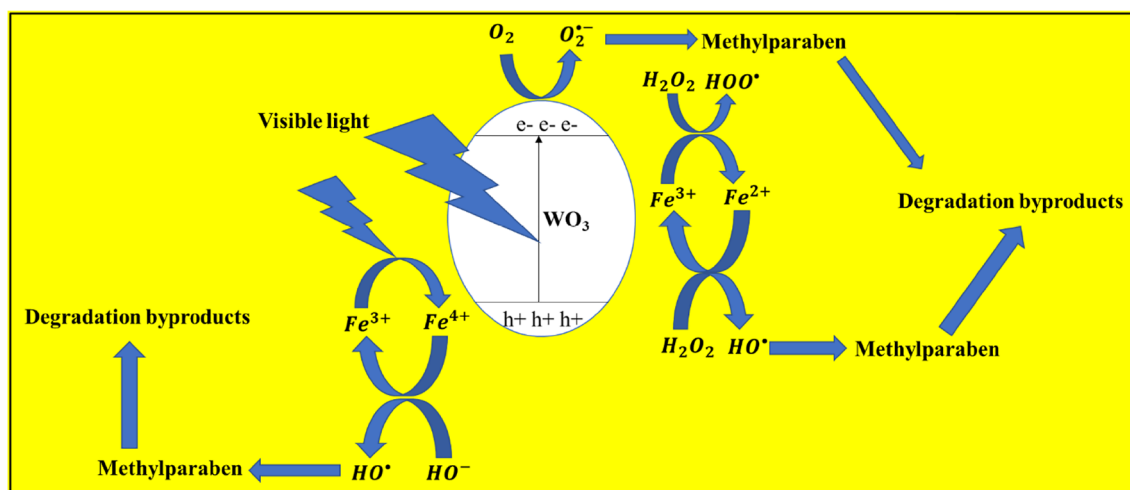
Eric Mwangi Ngigi<sup>1</sup> · Philiswa Nosizo Nomngongo<sup>1</sup> · Jane Catherine Ngila<sup>1</sup>

Received: 23 August 2018 / Accepted: 14 October 2018 / Published online: 30 October 2018  
© Springer Science+Business Media, LLC, part of Springer Nature 2018

## Abstract

Synthesis of  $\text{WO}_3$  and Fe-doped  $\text{WO}_3$  nanoparticles is done by use of Microwave irradiation technique. X-ray powder diffraction confirmed the formation of a monoclinic crystalline structure. The as-prepared samples are characterised by transmission electron microscope, Braunuer, Emmett and Teller, Raman spectroscopy, photoluminescence, X-ray photoelectron spectroscopy and ultraviolet diffuse reflectance spectroscopy. Confirmation of the morphology of the nanostructures showed ovoid-like form. The photocatalytic activity of  $\text{WO}_3$  and nominal percentage of Fe-doped  $\text{WO}_3$  (3, 5 and 10 wt%) are evaluated for the degradation of methylparaben (MeP) in aqueous solution after being irradiated with visible light. The results show that 5 wt% Fe- $\text{WO}_3$  is the best dopant in the photodegradation of MeP at 50.8% with  $\text{H}_2\text{O}_2$ . A chemometric model analysis is applied to estimate both individual and interaction factors that included pH, contact time, hydrogen peroxide ( $\text{H}_2\text{O}_2$ ) concentration and catalyst dosage. The optimal conditions at pH 3, 10 mg, 5 wt% Fe- $\text{WO}_3$  and 120 min are achieved.

## Graphical Abstract



**Keywords** Methylparaben · Microwave · Nanostructures · Photodegradation · Dopant

✉ Jane Catherine Ngila  
jcngila2015@gmail.com; jcngila@uj.ac.za

<sup>1</sup> Department of Applied Chemistry, University of Johannesburg, Doornfontein Campus, P.O. Box 17011, Johannesburg 2028, South Africa

## 1 Introduction

Water is a major necessity for all living organisms including human beings. Availability of clean water is of great concern due to the increased release of emerging pollutants into the

environment. As a result, this poses an enormous challenge, which is expected to increase due to high levels of industrialisation. The emerging pollutants are a group of chemicals that have been found in fresh waters because of various human activities. Among these are the personal care products (PCPs) that are used daily are released to the aquatic ecosystems in very low concentrations ranging from  $\mu\text{g L}^{-1}$  to  $\text{ng L}^{-1}$ . PCPs have not been previously considered as contaminants and they're hence required to be investigated and monitored because they are hazardous to aquatic life [1–4]. Parabens, a group of PCPs known as synthetic esters of  $\rho$ -hydroxybenzoic acid, are widely used as antimicrobial and preservatives because they are very effective in protecting pharmaceuticals, beverages and cosmetic products [5]. Examples of parabens include methylparaben (MeP), ethylparaben, propylparaben, butylparaben and benzyl paraben. MeP, a well-known endocrine disruptive chemical (EDC), is widely used as a bactericide and antimicrobial agent in cosmetic products, singly or combined with other agents [6, 7].

Emerging pollutants have been in existence for over a long period and have been determined and removed using conventional methods, mainly in wastewater treatment plants (WWTPs). The efficiency of treatment has been higher than 90% [8–10] in reducing the initial concentrations at the inlet of WWTPs. It has been found that benzylparaben, butylparaben, and isobutyl paraben have been found to have reduced using batch-activated sludge treatment [11] but the high instability of the main by-product  $\rho$ -hydroxybenzoic acid have been detected in high concentrations in both raw wastewater and effluents [12]. The drawbacks of the conventional irradiation methods suffer from pollutants being detected in low concentrations (in  $\text{ng L}^{-1}$ ) and partially removed. However, it has been observed that new derivatives of the parent compound are formed [8, 13, 14]. Initially, parabens were determined using separation solid phase extraction [17, 18], and quantification techniques such as micellar electrokinetic chromatography (MERC) [15, 16], capillary zone electrophoresis–ultra violet [17] due to their simplicity and effectiveness [18]. However, quantification analytical techniques used ranged from the high-performance liquid chromatography [19, 20] to the current and more advanced techniques including ultra-high performance liquid chromatography [21] and liquid chromatography–tandem mass spectrophotometer [22, 23] are commonly used. More so, gas chromatography–mass spectrophotometer [24, 25] comprising of a derivatisation step was used to determine the number of parabens in cosmetics, drugs, pharmaceuticals, and food, among others.

Photocatalysis is considered as one of the most promising technique in water treatment since it has a great potential utilizing green and sustainable solar energy in removing organic pollutants and harmful bacteria present in polluted water systems [26]. The photocatalytic

technology uses light and a photocatalyst in the decomposition of organic pollutant. Semiconductors have been used in photocatalysis for decomposing the organic pollutants rapidly and in an environmentally friendly manner [27–30]. However, another photocatalyst such as, tungsten trioxide ( $\text{WO}_3$ ) is a promising n-type semiconductor with an optical band gap ( $E_g$ ) of 2.8 eV that has received attention in recent times [31, 32].  $\text{WO}_3$  can be prepared using several methods such as; sol–gel [33], precipitation [34], hydrothermal [35] and glycothermal as reported by other researchers [36]. The only limitation it possesses is that it has poor photocatalytic activity due to the versatile wide bandgap and a result, the conduction band electrons cannot be efficiently trapped by oxygen to yield superoxide radicals [37–39].

Advanced oxidation processes have received significant attention in the removal of organic pollutant contaminants in aqueous solutions and wastewater [40]. The heterogeneous process has been proposed in Fenton reactions towards the degradation of organic pollutants [41]. Several authors have reported degradation of the phenol compound and its derivatives that includes Fenton [42], photo-Fenton [43], sono-Fenton [44] and  $\text{O}_3$ /Fenton [45].

Doping plays an indispensable part in tuning the band edge potential of photocatalyst by modifying its properties. The dopant ion incorporation has been employed in recent times to reduce the recombination of electrons and holes to enhance visible light absorption with the introduction of extra energy levels in doped material for better photocatalytic activity [28, 37, 46]. Transition metal (TM) doped semiconductor nanoparticles have been used due to their excellent dopants and catalytic activities with various metals such as Zn, Nb, Mn-doped  $\text{WO}_3$  has been prepared and reported [47–49] on reducing the band gap of  $\text{WO}_3$ . Iron has been investigated as a dopant ion in various reports for magnetic properties [39, 46, 50, 51] owing to its half-filled electronic configuration and can lead to conspicuous absorption in the visible light [52, 53]. Removal of MeP has been studied using different methods such as electrochemical [54], ozonation [55], photochemical [56], sonochemical [6]. Few researchers have reported on photocatalytic degradation of MeP using different photocatalysts [57–59]. Song et al. [60] and Zhang et al. [61] reported the synthesis of Fe-doped  $\text{WO}_3$  for catalysis and  $\text{NO}_2$  gas sensor respectively. To the best of our knowledge, no literature has been reported on the photodegradation of MeP with Fe-doped  $\text{WO}_3$ .

In view of the above, the aim of this study is to investigate the degradation of MeP for the first time using Fe-doped  $\text{WO}_3$  in combination with  $\text{H}_2\text{O}_2$  under the influence of visible light irradiation. The factors affecting (such as the addition of oxidant, sample pH, catalyst loading, degradation time and among others) the photocatalytic degradation of MeP were optimised using univariate and multivariate tools.

## 2 Experimental

### 2.1 Chemicals

Iron (III) nitrate nonahydrate (FeN<sub>3</sub>O<sub>9</sub>·9H<sub>2</sub>O) was obtained from Riedel-de Haën in Germany, Sodium hydroxide (NaOH), tungstic acid (≥ 99.0%) and Methyl-4-hydroxybenzoate (CAS:99-76-3) were obtained from Sigma-Aldrich (USA), nitric acid (65%) obtained from MCL (South Africa), absolute ethanol (99.9%) was obtained from Minema, (South Africa) and domestic microwave LG MS 283 MC 900 W. All chemicals were used as received. Deionised water was used in all experiments.

### 2.2 Material Synthesis

WO<sub>3</sub> nanoparticles were prepared by use of microwave used by Abhudhahir and Kandasamy [48] with modifications. Typically, 1 g of H<sub>2</sub>O<sub>4</sub>W was dissolved in 10 mL NaOH and 5 mL concentrated HNO<sub>3</sub> was added. 10 mL of deionised water was added to the acidic solution for quick response to microwave. The solution in a beaker was covered with a watch glass and quickly transferred to a microwave at a power of 200 W for 20 min. The powder obtained was washed severally with deionised water and ethanol to neutralise the acidity and dried in air at 100 °C for 1 h to remove water and excess ethanol. Heat treatment was done in air at 500 °C for 3 h in a muffle furnace. The Fe-doped WO<sub>3</sub> was synthesised by adding tungstic acid and Iron (III) nitrate nonahydrate at a nominal ratio (3, 5 and 10 wt%) followed by the above procedure. The heat treatment for Fe doped WO<sub>3</sub> was at 500 °C in the air for 3 h. The final products for WO<sub>3</sub> and Fe-doped WO<sub>3</sub> were pale yellow and brown respectively.

### 2.3 Characterisation

The crystallographic patterns of the as-prepared samples were characterised by powder X-ray diffractometer (Phillips X'Pert-PRO PANalytical) with Cu K $\alpha$  radiation ( $\lambda = 1.54060 \text{ \AA}$ ) with  $2\theta$  the scan range of 10°–90° with a step size of 0.0170 s<sup>-1</sup> at an acceleration voltage and applied a current of 40 kV and 40 mA, respectively. Raman spectra were recorded on a Raman spectrometer (WITec) operating with a 531.5 nm diode laser. The morphologies and particle sizes were determined with scanning electron microscope (Tescan). Transmission electron microscope (TEM) and high-resolution transmission electron microscope (HRTEM) images were obtained using Jeol, JEM-2100 with an acceleration voltage of 200 kV. The surface area was evaluated using nitrogen absorption–desorption isotherms and adsorption data at –197 °C using Brunauer–Emmett–Teller (BET)

method (Micrometrics ASAP 2020). X-ray photoelectron spectroscopy (XPS) measurements were performed at room temperature using a SPECS PHOIBOS 150 electron energy analyser, and a Al–K $\alpha$  monochromatized photon source ( $h\nu = 1486.71 \text{ eV}$ ). The overall energy resolution was set to 0.6 eV for all spectra presented in this work. Photoluminescence (PL) was recorded using Perkin-Elmer LS 45 Fluorescence spectrometer with an excitation wavelength of 270 nm and UV–Vis diffuse reflection spectrophotometer (UV–DRS, Shimadzu 2450) using BaSO<sub>4</sub> as a reference.

### 2.4 Experimental Procedure

MeP stock solution of 100 ppm was prepared using deionised water and was stored in the dark at 4 °C. The working standard solutions were prepared from the stock solutions to the desired concentrations of 10 ppm and used throughout the experiments.

The pH values of 3, 6 and 9 were adjusted by addition of 0.1 M HCl or 0.1 M NaOH throughout the experiment. A volume of 30 mL aqueous MeP solution was introduced into the vessel and required an amount of the catalyst and 10 mM H<sub>2</sub>O<sub>2</sub> were introduced as per the experimental design. Before irradiation, the solution, H<sub>2</sub>O<sub>2</sub> and catalyst were initially mixed in the dark for 30 min for adsorption–desorption to reach equilibrium. For the degradation experiments, aliquots of ~2.5 mL were sampled at different intervals, filtered and centrifuged at 7000 rpm for 10 min. The UV–Vis spectra absorbance were recorded using Shimadzu 2450 spectrophotometer.

### 2.5 Photoreactor and Light Source

The photocatalytic performers of both as-prepared samples of WO<sub>3</sub> and Fe-doped WO<sub>3</sub> towards degradation of MeP were evaluated using a photo-reactor equipped with Xenon lamp capable of emitting 1 SUN (1000W/m<sup>2</sup>) equivalent to solar light equipped with a UV cut-off filter ( $\lambda > 420 \text{ nm}$ ) was used in this experiment.

### 2.6 Experimental Data Design Analysis

The chemometric analysis was performed using a STATISTICA software version 13.

## 3 Results and Discussion

### 3.1 XRD Analysis

The crystallographic study of the products was characterised by X-ray diffraction (XRD), as shown in Fig. 1. The XRD spectra of pure WO<sub>3</sub> and Fe-doped WO<sub>3</sub>

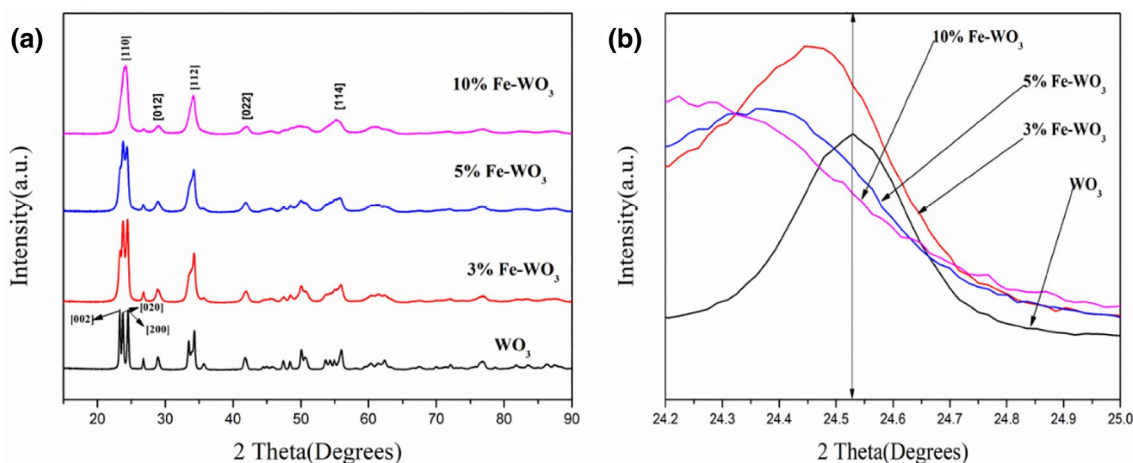


**Fig. 1** **a** XRD patterns for as-prepared samples and **b** cross-section of the plane [020]

**Table 1** Crystallite size of the prepared samples

Sample	Crystallite size (nm)
WO <sub>3</sub>	10.13
3 wt% Fe-WO <sub>3</sub>	5.06
5 wt% Fe-WO <sub>3</sub>	7.59
10 wt% Fe-WO <sub>3</sub>	6.07

were prepared and shown in Fig. 1a. From the spectra, it shows that the structure of WO<sub>3</sub> nanoparticles was monoclinic (ICDD 04-005-4272, space group: P21/n with lattice parameters of  $a = 7.2970$  Å,  $b = 7.5390$  Å and  $c = 7.6880$  Å). With increasing doping of Fe, no other impurities could be detected in the spectra indicating successful incorporation of Fe into the crystal lattice with the overall crystal structure being monoclinic despite an increase of Fe<sup>3+</sup> ions from 3 to 10%. Figure 1b shows cross sectional area of peak [020] where Fe doped WO<sub>3</sub> shifting lower diffraction angles indicating the incorporation of Fe<sup>3+</sup> into the WO<sub>3</sub> crystal lattice and this is due to the fact that Fe<sup>3+</sup> (radius 0.064 nm) is almost equal to W<sup>6+</sup> (0.062 nm) [49].

The crystallite sizes  $D$  of both pure and Fe-doped WO<sub>3</sub> were calculated using Debye–Scherrer in Eq. 1 with data shown in Table 1 tabulated using Bragg's angle at  $2\theta = 24.5$ .

$$D = \frac{0.9\lambda}{\beta \cos\theta} \quad (1)$$

From the results obtained with Fe ions doped in WO<sub>3</sub>, the average crystallite sizes between the lowest (3 wt%) and highest doping concentrations (10 wt%) were marginally reduced.

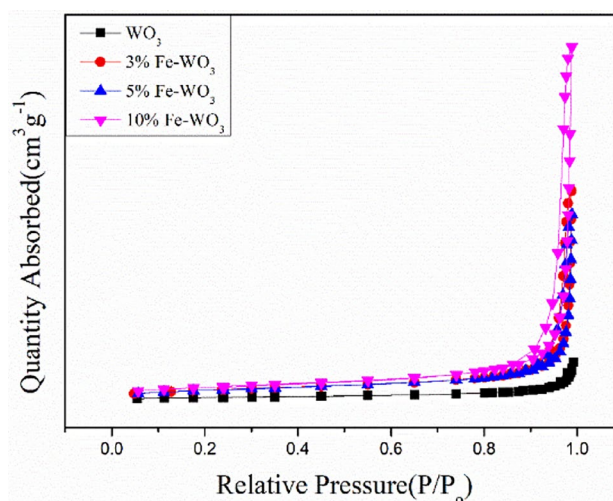


**Fig. 2** Nitrogen adsorption–desorption isotherms curves

### 3.2 B.E.T. Analysis

The isotherm of WO<sub>3</sub> and Fe-doped WO<sub>3</sub> in Fig. 2 can be categorised as Type II [62] and H3 hysteresis loop observed in relative pressure of between 0.9 and 1.0 indicates a mesoporous material [60]. The BET surface areas of as-prepared WO<sub>3</sub>, 3% wt, 5% wt, and 10% wt Fe-doped WO<sub>3</sub> were 5.7, 16.1, 15.4 and 19.8 m<sup>2</sup> g<sup>-1</sup>, respectively. As from the figures indicated the surface area increases as the doping increases indicating an increase of large active sites for photocatalytic activity for doped samples.

### 3.3 Optical Properties

UV–Vis diffuse reflectance spectroscopy was used to study the optical properties of pristine and Fe-doped WO<sub>3</sub>

nanoparticles, as shown in Fig. 3. Figure 3a indicates the absorbance of as-prepared samples in which it indicates a blue shift with an increase of Fe doping from 450 nm (WO<sub>3</sub>) to 512 nm (10% Fe-doped WO<sub>3</sub>). The optical absorption coefficient obeys the indirect-band gap, as shown in Eq. (2):

$$(\alpha h\nu)^2 = A(h\nu - E_g) \quad (2)$$

where  $\alpha$  is the absorption coefficient,  $h$  is the Plank's constant,  $\nu$  is the frequency of light,  $E_g$  is the band gap and  $A$  is the constant. The band gap was determined from the intercept of  $\alpha h\nu^2$  versus  $h\nu$  curves and from the calculations, the band gap of WO<sub>3</sub> was found to be 2.48 eV. With the increase of Fe doping from 3 to 10 wt% a decrease in band gap was observed from 2.48 to 2.08 eV, as shown in Fig. 3b. The observations show that with the introduction of iron doping indicates that the iron atoms are located at the donor level above valence band of WO<sub>3</sub>. It could be attributed to sp-d spin interactions between band electrons and localised d electrons of the TM substituting the cation [46, 50].

### 3.4 TEM Analysis

In order to determine the actual morphologies of the as-prepared samples of WO<sub>3</sub> and Fe-doped WO<sub>3</sub> samples TEM and HRTEM images, as shown in Fig. 4. The TEM images showed the ovoid-like structure of undoped WO<sub>3</sub> due to aggregation or overlapping of small particles, as shown in Fig. 4a. Figure 4b indicates smaller structures of Fe-doped WO<sub>3</sub> indicating successful incorporation of Fe ions into the crystal structure of WO<sub>3</sub> and from the results shown from Table 1 confirming that the smaller the size the greater the surface area and in which the shape was not necessarily altered [51]. Figure 4c shows the EDS indicating the elements W, O, and Fe. Meanwhile, Fig. 4d is HRTEM showing

a well-defined crystalline structure with interplanar spacing calculated as 0.39 nm indexing to [020] equivalents to undoped WO<sub>3</sub> consistent with XRD results.

### 3.5 Raman Analysis

Figure 5 shows Raman spectra of both pristine WO<sub>3</sub> and Fe-doped WO<sub>3</sub> indicating the stretching and bending modes of WO<sub>3</sub> with no extra Fe–O bond. Frequencies 200–400 cm<sup>-1</sup> indicates O–W–O bending modes and peak at 272 cm<sup>-1</sup> corresponding to the O–W–O stretching mode of the bridging oxygen while frequencies between 600 and 900 cm<sup>-1</sup> relate to W–O stretching modes [63]. The peaks 272, 722 and 811 cm<sup>-1</sup> indicate a probable mixture of  $\gamma$  and  $\delta$  monoclinic phases at room temperature [63]. The characteristic peaks of WO<sub>3</sub> gradually decreased their intensity and shifted to lower wavenumbers with an increase in iron content from 3 to 10 wt% resulting in the occupation of substitutional sites of WO<sub>3</sub>.

### 3.6 Photoluminescence (PL) Studies

Figure 6 shows the PL emissions of as-prepared WO<sub>3</sub> and Fe-doped WO<sub>3</sub> of different wt% at room temperature. The samples were excited at 270 nm in which they displayed emission centred at 537 nm. The small emission peak at 589 nm could be attributed to the oxygen deficiency peak. After doping with different wt% of Fe the emission displayed the same emission spectra but with reduced intensities. This phenomenon can be attributed to an increase in defects resulting in displacing W<sup>6+</sup> with Fe<sup>3+</sup> [49]. In general, the lower the PL the lower the recombination of the photogenerated electrons and holes [64] indicating that 5 wt% Fe-doped WO<sub>3</sub> shows the best photocatalytic activity

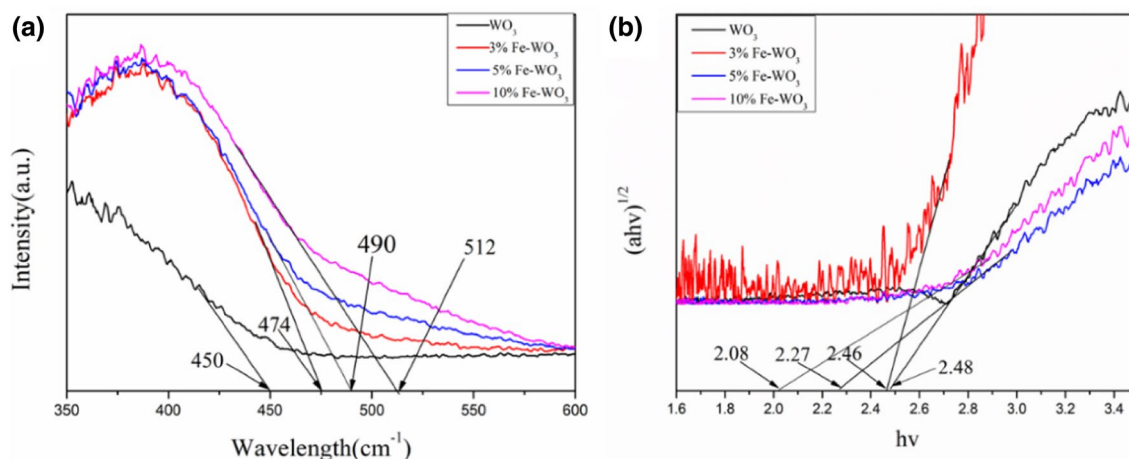


**Fig. 3** a UV-Vis Diffuse reflectance spectra and b Tauc plots for WO<sub>3</sub>, 3 wt%, 5 wt% and 10 wt% Fe-doped WO<sub>3</sub> respectively

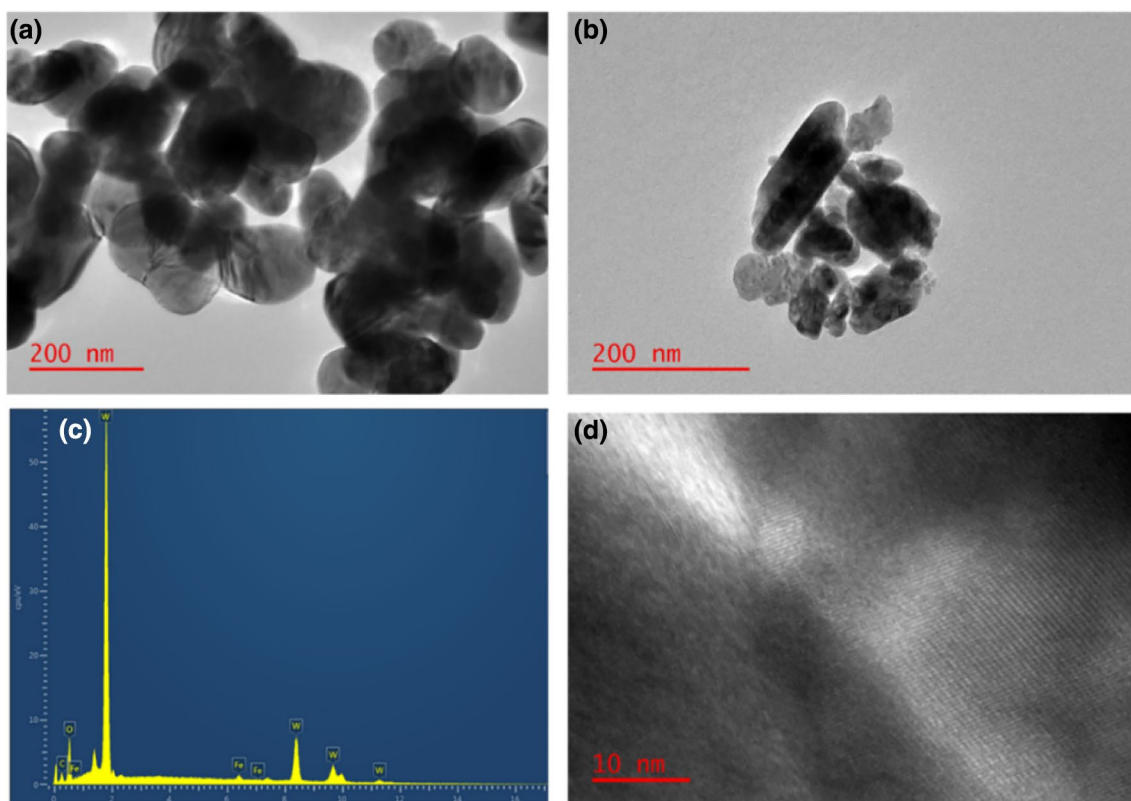


**Fig. 4** TEM images of  $\text{WO}_3$  (a), 5 wt% Fe-doped  $\text{WO}_3$  (b), EDS of 5 wt% Fe-doped  $\text{WO}_3$  (c) and HRTEM image of 5 wt% Fe-doped  $\text{WO}_3$  (d)

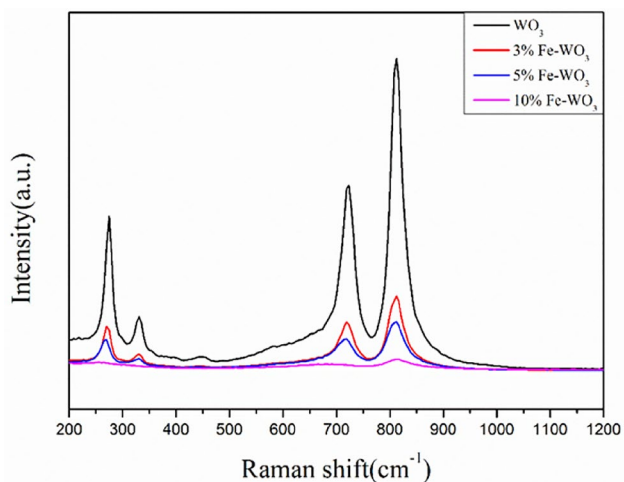


**Fig. 5** Raman spectra of pure  $\text{WO}_3$  and Fe-doped  $\text{WO}_3$

for degradation having lower recombination rate in comparison with the others.

### 3.7 X-Ray Photoelectron Spectroscopy (XPS)

XPS spectra for the as-prepared 5 wt% Fe-doped  $\text{WO}_3$  was presented to determine the oxidation states and elemental

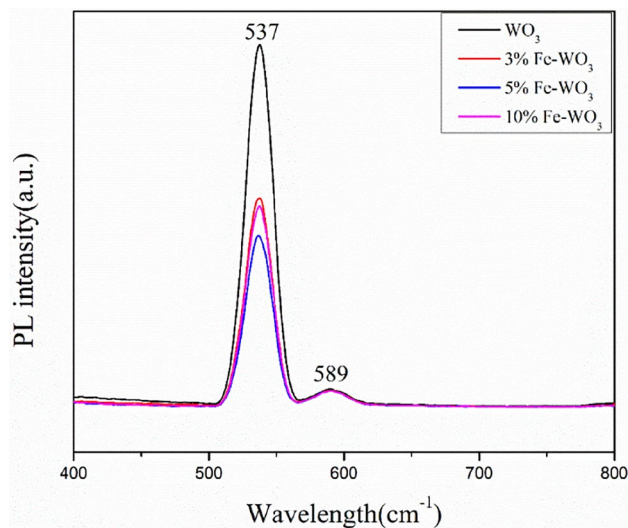


**Fig. 6** PL spectra of undoped  $\text{WO}_3$  and Fe-doped  $\text{WO}_3$  at different wt%

composition for each member of the catalyst, as shown in Fig. 7. Figure 7a depicts the presence of C, W, Fe and O elements with a small Na peak may be attributed to precursors used in synthesis. Figure 7b shows the deconvoluted Fe 2p spectrum with two peaks at  $\sim 712$  and  $\sim 726$  eV

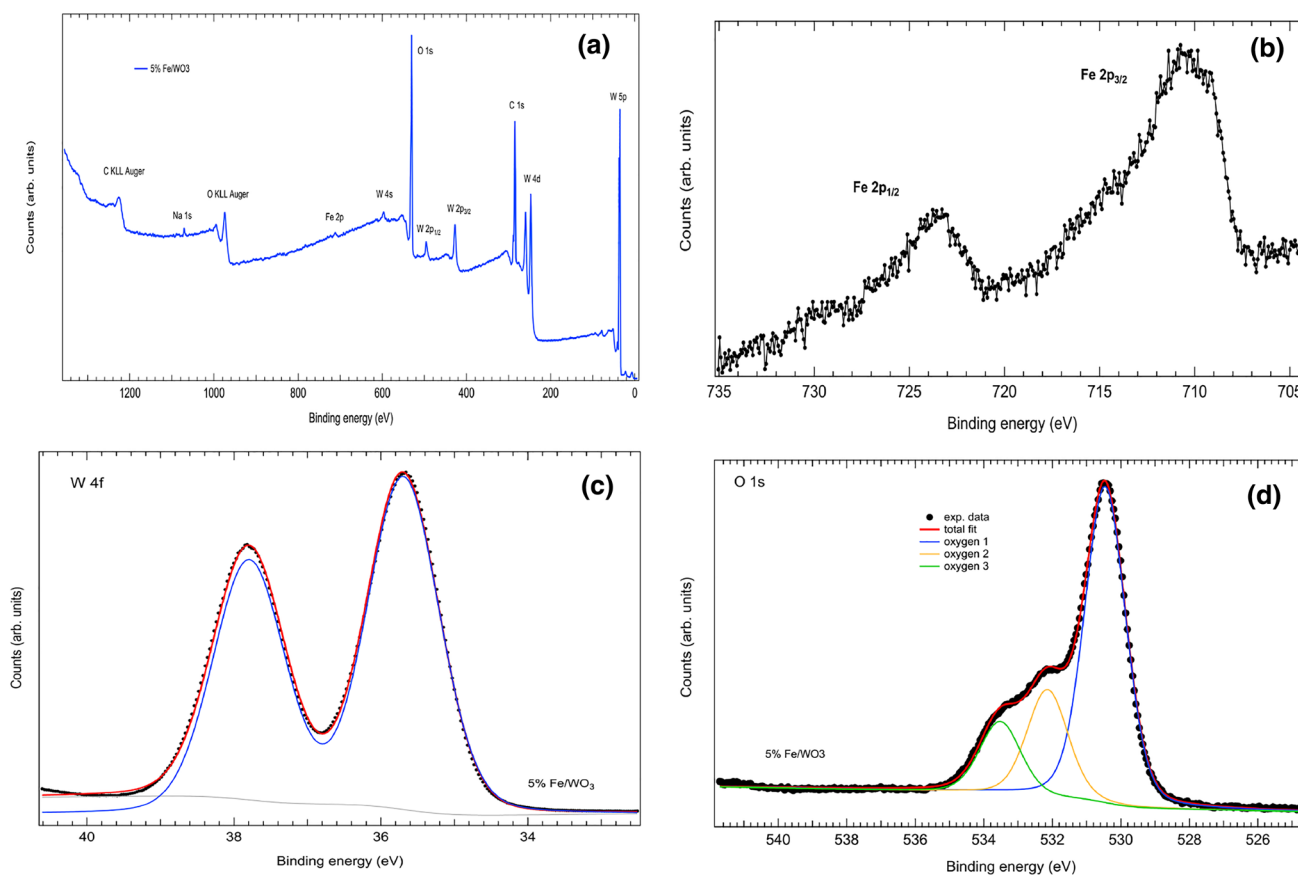


**Fig. 7** XPS spectra of 5% Fe–WO<sub>3</sub> photocatalyst obtained by microwave synthesis: **a** survey scan of 5% Fe–WO<sub>3</sub>, **b** Fe 2p, **c** W 4f and **d** O 1s

corresponding to Fe 2p<sub>3/2</sub> and Fe 2p<sub>1/2</sub> respectively resulting from Fe<sup>3+</sup> ions incorporated into WO<sub>3</sub> matrix [65]. Figure 7c represents the deconvoluted W 4f spectrum which has two pronounced peaks 35.4 and 37.6 eV belongs to W 4f<sub>7/2</sub> and W 4f<sub>5/2</sub> indicating the presence of WO<sub>3</sub> in the catalyst [61]. It is clear from the peaks that W<sup>6+</sup> is the main state on the surface. The deconvoluted O 1s spectrum of ovoid-like WO<sub>3</sub>, as shown in Fig. 7d indicates one large hump and two minor humps fitted with three sub-peaks at 530 eV representing O<sup>2-</sup>, O<sup>-</sup>, O<sub>2</sub><sup>-</sup> ions in oxygen deficient regions, while 532 eV could be assigned to either vacancies, defects or adsorbed oxygen within WO<sub>3</sub> matrix and 533.6 eV adsorbed water on the surface [65].

### 3.8 Catalytic Results

#### 3.8.1 Catalyst Selection

MeP is known to be resistant to either cold or hot water and in this experiment, the effect was insignificant as there was no change in degradation [66]. The photocatalytic degradation of MeP was investigated using different catalysts at pH 6.5, as shown in Fig. 8. The preliminary experiments were

performed in the absence of a catalyst (that is, photolysis) and it can be seen in Fig. 8a that there was no significant change in the MeP. These observations verified the high photochemical resistance of MeP towards photodegradation. With the addition of H<sub>2</sub>O<sub>2</sub>, there was a weak degradation because the light could not produce enough hydroxyl radicals (HO<sup>•</sup>). Figure 8b shows that the % degradation of MeP. The initial results indicated that with an increase of Fe doping the % degradation increases. From the results shown in Fig. 8b, 5 wt% Fe-doped WO<sub>3</sub> displayed better photocatalyst than the rest indicating a better charge separation efficiency as indicated from PL studies (Fig. 6). Therefore, was used for further investigations.

#### 3.8.2 Effect of H<sub>2</sub>O<sub>2</sub> Concentrations on Photocatalytic Activity of Fe-doped WO<sub>3</sub>

The addition of an oxidant expected to accelerate the heterogeneous photocatalytic degradation of organic pollutants. Hydrogen peroxide as an electron acceptor is a key parameter in Fenton or Fenton-like oxidation process [67, 68]. In photocatalytic degradation system of MeP, the catalytic mechanism of H<sub>2</sub>O<sub>2</sub> molecules over the surface of Fe-doped

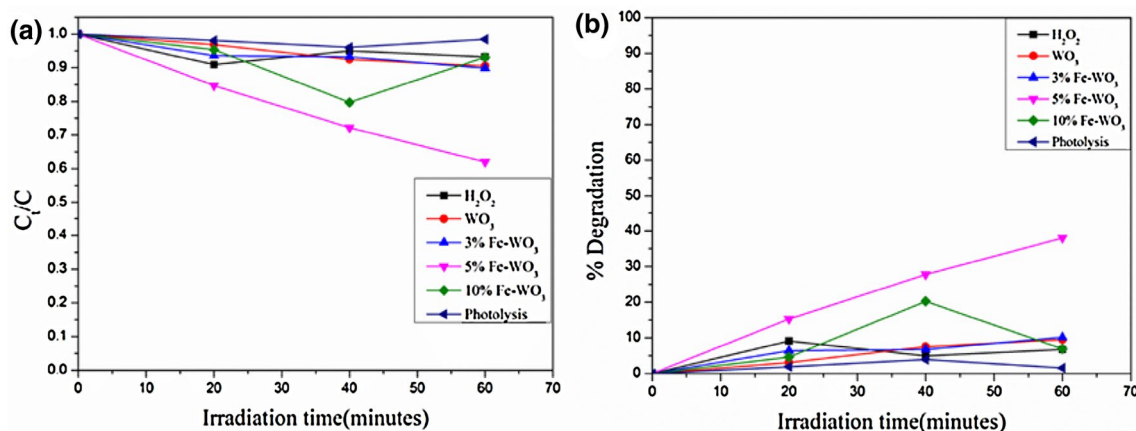


**Fig. 8** a Kinetic profiles comparison of methylparaben with photolysis,  $H_2O_2$ ,  $WO_3$  and Fe-doped  $WO_3$  (3% wt, 5% wt and 10% wt) at pH 6.5 and b comparison % degradation

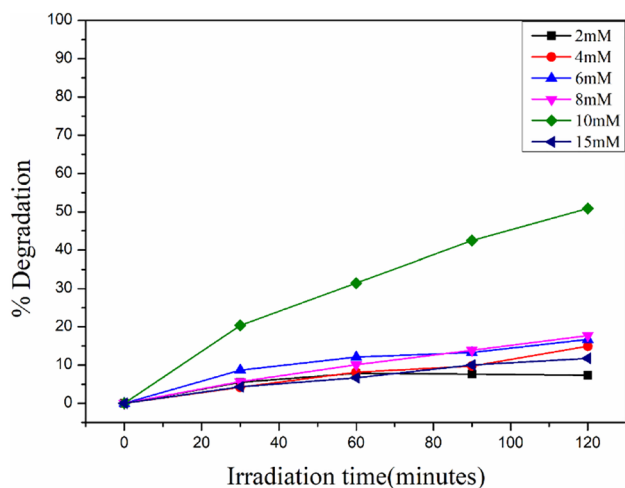
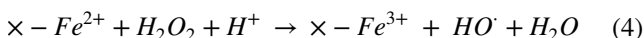
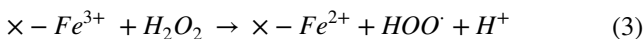


**Fig. 9** Effects of  $H_2O_2$  concentration on the degradation of methylparaben [initial concentration 10 ppm, pH 3 and catalyst 10 mg (5 wt% Fe-doped  $WO_3$ )]

$WO_3$  is analogous to Fenton-type mechanism.  $Fe^{3+}$  ions on the surface of Fe-doped  $WO_3$  could react with  $H_2O_2$  to produce  $HO\cdot$  can demonstrated using by Eqs. 3 and 4 [69]:

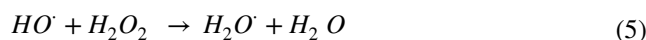


In which  $\times$  represents the surface of  $WO_3$ . For this reason, the effect of different concentration of  $H_2O_2$  (2–15 mM) on the photodegradation of MeP was investigated and the results are presented in Fig. 9. It can be seen from the results that concentrations below 10 mM showed slow degradation process due to less production of enough hydroxyl radicals for oxidation. However, at higher concentration of 15 mM, a decrease in degradation was observed which may be due to

**Table 2** Multivariate optimisation: factorial design matrix and analytical response (% degradation)

Expt	pH	Time	Dosage	% Degradation
1	3	30	10	25.7
2	9	30	10	15.6
3	3	120	10	50.8
4	9	120	10	30.5
5	3	30	50	16.9
6	9	30	50	12.1
7	3	120	50	48.2
8	9	120	50	1.35
9	6	75	30	21.3
10	6	75	30	14.9
11	6	75	30	10.6

excess of hydroxyl radicals that may react with excess  $H_2O_2$  thus becoming a scavenger [1] and hence retards the degradation efficiency process according to the Eq. 5. Therefore, 10 mM was used for further investigation.



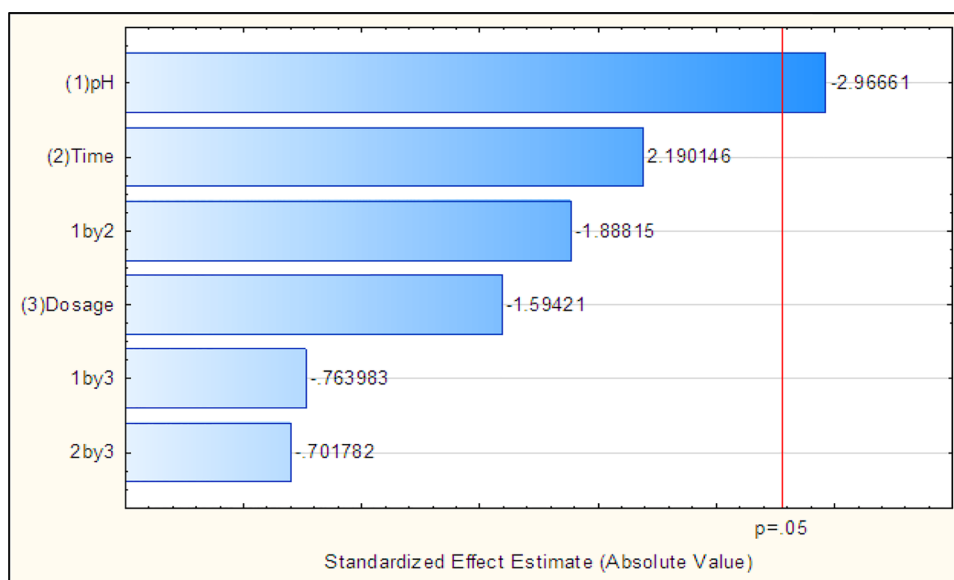
### 3.8.3 Multivariate Optimisation

The effect of factors affecting the photodegradation process was investigated using two-level full factorial design with three independent variables and three central points. This resulted in a total of 11 experiments with all possible combinations of the actual values. The factorial design matrix and analytical response (% degradation) are shown in Table 2. Catalyst loading and contact time have less significance among the three factors.

Figure 10 presents the Pareto chart of the standardised effects used to investigate the variables that had a significant



**Fig. 10** Pareto chart for standardised effect of 50% MeP degradation removal [10 mg L<sup>-1</sup> (30 mL), irradiation time 120 min, pH 3 and 10 mg]



influence on the analytical response (% degradation). It can be observed that the bar length of the sample pH value surpassed the vertical significance line (95% confidence intervals). This means that this variable was statistically important. In addition, the other variables and the interactions were not significant at 95% at a confidence level. In this experiment, the pH range selected were 3, 6 and 9 to determine the efficiency of the photocatalyst on degradation of MeP. The dependency of pH is on the surface charge of the photocatalyst, the net charge of pollutant and a number of hydroxyl radicals produced [66]. Most pollutants in aquatic systems are mainly dependent on pH and their respective dissociation constants and this case MeP is no exception as is dependent on certain pH range and having pKa 8.3. If  $\text{pH} < \text{pKa}$ , MeP is in molecular state and vice versa. From the experimental data (Table 2) the best pH for 5 wt% Fe-doped WO<sub>3</sub> was 3. This is due to the fact that the surface charge of WO<sub>3</sub> is almost comparable to its point-of-zero-charge of 2.5 [70] in which electrons valence bands can be able to convert H<sub>2</sub>O<sub>2</sub> to hydroxyl radicals that can degrade MeP. In addition, it was observed that the algebraic sign for sample pH effect was negative. This demonstrated that sample pH lower than the maximum levels should be used.

In general, dosage loading plays a critical role in the degradation of organic pollutants. The selected 5 wt% Fe-doped WO<sub>3</sub> catalyst was varied between 10 mg, 30 mg, and 50 mg respectively. From values shown on Table 2 different values were obtained with pH variation, what was noticed was that at a low dosage and high contact time, the degradation was higher indicating that there were more active sites on the surface of the catalyst. Figure 9 showed that the effect of time on degradation did give some semblance of the difference from the values tabulated in Table 2, which indicated that long contact time increased the contact of the surface

of photocatalyst active sites for photon absorption. The optimal conditions for the highest photocatalytic efficiency of MeP estimated in Fig. 10 is as follows: pH 3, 10 mg, 5 wt% Fe-doped WO<sub>3</sub> and 120 min with 50.8% degradation of MeP. Several studies have reported on removal of MeP using different photocatalysts where Kumar et al. [68] used Fe<sub>3</sub>O<sub>4</sub>/BiVO<sub>4</sub> with biochar and achieved 97.4% MeP removal, while Xiao et al. [58] achieved 66.8% mineralization when  $\beta$ -Bi<sub>2</sub>O<sub>3</sub> was utilized. Few reported on use of H<sub>2</sub>O<sub>2</sub> with photocatalyst in removal of MeP where Velegraki et al. [71] reported degradation of MeP with H<sub>2</sub>O<sub>2</sub> using carbon-doped Kronos Vlp 7000 and Kronos Vlp 7001 powders. They achieved a 57% and 62% removal of MeP for the respective carbon-doped powders.

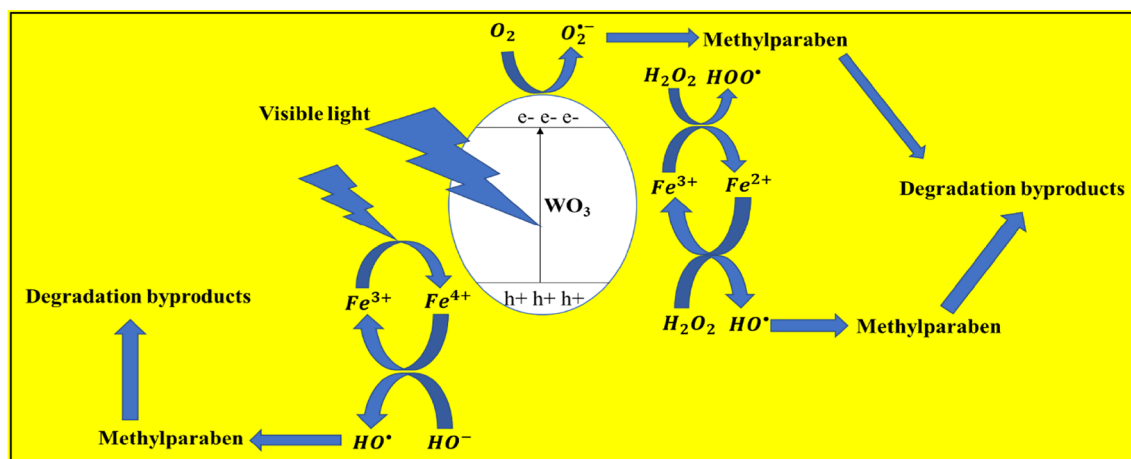
The multivariate experimental design showed more success than univariate in that it gave a reasonable model of interactions between various factors.

### 3.9 Photocatalytic Degradation Mechanism

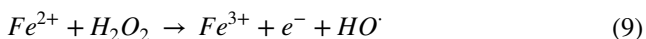
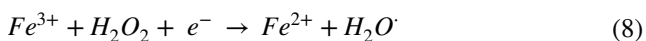
To understand the roles of electrons, holes and HO<sup>•</sup> involvement in degradation of MeP at best doping concentration under visible light irradiation. Scheme 1 shows the overall photocatalytic activity performed at 5 wt% Fe-doped WO<sub>3</sub> photocatalyst for degradation of MeP at pH value of 3, 10 mM H<sub>2</sub>O<sub>2</sub> and dosage of 10 mg.

The Fe<sup>3+</sup> ions act as a sink in which they trap and transfer electrons and holes to minimise recombination of photo-excited holes and electrons [60] as can be shown by the following Eq. 5 to 10 in conduction band region

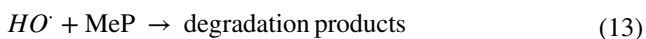




**Scheme 1** Proposed charge separation and photocatalytic degradation mechanism with Fe-doped  $\text{WO}_3$  and  $\text{H}_2\text{O}_2$



In the valence band region, the  $\text{Fe}^{3+}$  ions are oxidised by visible light to produce  $\text{Fe}^{4+}$  ions according to Eq. 11 to 13



## 4 Conclusion

The as-prepared  $\text{WO}_3$  and Fe-doped  $\text{WO}_3$  nanostructures were successfully prepared using microwave irradiation method. From the results of XRD, Raman, XPS and TEM, Fe was successfully incorporated into  $\text{WO}_3$  crystal lattice without formation of iron oxide impurities. In comparison with undoped  $\text{WO}_3$ , 5 wt% Fe-doped  $\text{WO}_3$  showed a better photocatalytic degradation of MeP. The PL spectra indicated that doping with 5 wt% showed a lower recombination rate as compared to undoped, 3 wt% and 10 wt%. A chemometric analysis method was proposed and applied successfully to the photocatalytic process where the optimal conditions were obtained through the Pareto chart. Both individual and interaction factors were taken into considerations. 10 mg, pH 3, 10 mM  $\text{H}_2\text{O}_2$  and duration of 120 min was found as the best conditions for the degradation of MeP. According to experimental results, the mechanism of hydroxyl radical presented in the heterogeneous system revealed the efficiency and enhancement of iron doping  $\text{WO}_3$  on visible light activity of the organic pollutant.

**Acknowledgements** The authors wish to acknowledge the Water Research Commission (Grant No. K5/2563) and the Department of Applied Chemistry at the University of Johannesburg for partial funding. The authors also thank the Spectra Analytical Facility, the University of Johannesburg for the availability of XRD, SEM, TEM analysis and Department of Physics for XPS analysis.

**Conflict of interest** The authors declare that there is no conflict of interest regarding the publication of this paper.

## References

- Jiang J-Q, Zhou Z, Sharma VK (2013) Occurrence, transportation, monitoring and treatment of emerging micro-pollutants in waste water—a review from global views. *Microchem J* 110:292–300
- Carlos L, Mártire DO, Gonzalez MC, Gomis J, Bernabeu A, Amat AM, Arques A (2012) Photochemical fate of a mixture of emerging pollutants in the presence of humic substances. *Water Res* 46(15):4732–4740
- Muñoz I, José Gómez M, Molina-Díaz A, Huijbregts MAJ, Fernández-Alba AR, García-Calvo E (2008) Ranking potential impacts of priority and emerging pollutants in urban wastewater through life cycle impact assessment. *Chemosphere* 74(1):37–44
- Vulliet E, Cren-Olivé C (2011) Screening of pharmaceuticals and hormones at the regional scale, in surface and groundwaters intended to human consumption. *Environ Pollut* 159(10):2929–2934
- Alcudia-León MC, Lucena R, Cárdenas S, Valcárcel M (2013) Determination of parabens in waters by magnetically confined hydrophobic nanoparticle microextraction coupled to gas chromatography/mass spectrometry. *Microchem J* 110:643–648
- Sasi S, Rayaroth MP, Devadasan D, Aravind UK, Aravinda kumar CT (2015) Influence of inorganic ions and selected emerging contaminants on the degradation of methylparaben: a sonochemical approach. *J Hazard Mater* 300:202–209
- Lam S-M, Sin J-C, Zuhairi Abdullah A, Rahman Mohamed A (2013) Green hydrothermal synthesis of ZnO nanotubes for photocatalytic degradation of methylparaben. *Mater Lett* 93:423–426
- Trenholm RA, Vanderford BJ, Drewes JE, Snyder SA (2008) Determination of household chemicals using gas chromatography

- and liquid chromatography with tandem mass spectrometry. *J Chromatogr A* 1190(1–2):253–262
9. Yu Y, Huang Q, Wang Z, Zhang K, Tang C, Cui J, Feng J, Peng X (2011) Occurrence and behavior of pharmaceuticals, steroid hormones, and endocrine-disrupting personal care products in wastewater and the recipient river water of the Pearl River Delta, South China. *J Environ Monit* 13(4):871–878
  10. Andersen HR, Lundsbye M, Wedel HV, Eriksson E, Ledin A (2007) Estrogenic personal care products in a greywater reuse system. *Water Sci Technol* 56(12):45–49
  11. Yamamoto H, Watanabe M, Hirata Y, Nakamura Y, Nakamura Y, Kitani C, Sekizawa J, Uchida M, Nakamura H, Kagami Y, Koshio M, Hirai N, Tatarazako N (2007) Preliminary ecological risk assessment of butylparaben and benzylparaben-1. Removal efficiency in wastewater treatment, acute/chronic toxicity for aquatic organisms, and effects on medaka gene expression. *Environ Sci* 14(Suppl):73–87
  12. Blanco E, Casais MdC, Mejuto MdC, Cela R (2009) Combination of off-line solid-phase extraction and on-column sample stacking for sensitive determination of parabens and p-hydroxybenzoic acid in waters by non-aqueous capillary electrophoresis. *Anal Chim Acta* 647(1):104–111
  13. Haman C, Dauchy X, Rosin C, Munoz J-F (2015) Occurrence, fate and behavior of parabens in aquatic environments: a review. *Water Res* 68:1–11
  14. Lee H-B, Peart TE, Svoboda ML (2005) Determination of endocrine-disrupting phenols, acidic pharmaceuticals, and personal-care products in sewage by solid-phase extraction and gas chromatography–mass spectrometry. *J Chromatogr A* 1094(1–2):122–129
  15. Driouch R, Takayanagi T, Oshima M, Motomizu S (2000) Separation and determination of haloperidol, parabens and some of their degradation products by micellar electrokinetic chromatography. *J Chromatogr A* 903(1–2):271–278
  16. Huang H-Y, Lai Y-C, Chiu C-W, Yeh J-M (2003) Comparing micellar electrokinetic chromatography and microemulsion electrokinetic chromatography for the analysis of preservatives in pharmaceutical and cosmetic products. *J Chromatogr A* 993(1–2):153–164
  17. Dolzan MD, Spudeit DA, Azevedo MS, Costa ACO, de Oliveira MAL, Mücke GA (2013) A fast method for simultaneous analysis of methyl, ethyl, propyl and butylparaben in cosmetics and pharmaceutical formulations using capillary zone electrophoresis with UV detection. *Anal Methods* 5(21):6023–6029
  18. Márquez-Sillero I, Aguilera-Herrador E, Cárdenas S, Valcárcel M (2010) Determination of parabens in cosmetic products using multi-walled carbon nanotubes as solid phase extraction sorbent and corona-charged aerosol detection system. *J Chromatogr A* 1217(1):1–6
  19. Noorashikin MS, Mohamad S, Abas MR (2014) Extraction and determination of parabens in water samples using an aqueous two-phase system of ionic liquid and salts with beta-cyclodextrin as the modifier coupled with high performance liquid chromatography. *Anal Methods* 6(2):419–425
  20. Zgola-Grzeskowiak A, Werner J, Jeszka-Skowron M, Czarzynska-Goslinska B (2016) Determination of parabens in cosmetic products using high performance liquid chromatography with fluorescence detection. *Anal Methods* 8(19):3903–3909
  21. Gonzalez-Hernandez P, Pino V, Ayala JH, Afonso AM (2015) A simplified vortex-assisted emulsification microextraction method for determining personal care products in environmental water samples by ultra-high-performance liquid chromatography. *Anal Methods* 7(5):1825–1833
  22. Cao S, Liu Z, Zhang L, Xi C, Li X, Wang G, Yuan R, Mu Z (2013) Development of an HPLC-MS/MS method for the simultaneous analysis of six kinds of parabens in food. *Anal Methods* 5(4):1016–1023
  23. Lu L, Xiong W, Li X, Lv S, Tang X, Chen M, Zou Z, Lin Z, Qiu B, Chen G (2014) Determination of the migration of eight parabens from antibacterial plastic packaging by liquid chromatography–electrospray ionization–tandem mass spectrometry. *Anal Methods* 6(7):2096–2101
  24. Shanmugam G, Ramaswamy BR, Radhakrishnan V, Tao H (2010) GC–MS method for the determination of paraben preservatives in the human breast cancerous tissue. *Microchem J* 96(2):391–396
  25. Fan X, Kubwabo C, Rasmussen P, Jones-Otazo H (2010) Simultaneous quantitation of parabens, triclosan, and methyl triclosan in indoor house dust using solid phase extraction and gas chromatography–mass spectrometry. *J Environ Monit* 12(10):1891–1897
  26. Che H, Liu C, Hu W, Hu H, Li J, Dou J, Shi W, Li C, Dong H (2018) NGQD active sites as effective collectors of charge carriers for improving the photocatalytic performance of Z-scheme g-C<sub>3</sub>N<sub>4</sub>/Bi<sub>2</sub>WO<sub>6</sub> heterojunctions. *Catal Sci Tech* 8(2):622–631
  27. Ye L, Su Y, Jin X, Xie H, Zhang C (2014) Recent advances in BiOX (X = Cl, Br and I) photocatalysts: synthesis, modification, facet effects and mechanisms. *Environ Sci* 1(2):90–112
  28. Dong S, Feng J, Fan M, Pi Y, Hu L, Han X, Liu M, Sun J, Sun J (2015) Recent developments in heterogeneous photocatalytic water treatment using visible light-responsive photocatalysts: a review. *RSC Adv* 5(19):14610–14630
  29. Wen Z, Wu W, Liu Z, Zhang H, Li J, Chen J (2013) Ultrahigh-efficiency photocatalysts based on mesoporous Pt-WO<sub>3</sub> nanohybrids. *Phys Chem Chem Phys* 15(18):6773–6778
  30. Che H, Che G, Dong H, Hu W, Hu H, Liu C, Li C (2018) Fabrication of Z-scheme Bi<sub>3</sub>O<sub>4</sub>Cl/g-C<sub>3</sub>N<sub>4</sub> 2D/2D heterojunctions with enhanced interfacial charge separation and photocatalytic degradation various organic pollutants activity. *Appl Surf Sci* 455:705–716
  31. Adhikari S, Sarkar D (2014) Hydrothermal synthesis and electrochromism of WO<sub>3</sub> nanocuboids. *RSC Adv* 4(39):20145–20153
  32. Qian J, Zhao Z, Shen Z, Zhang G, Peng Z, Fu X (2016) Oxide vacancies enhanced visible active photocatalytic W<sub>19</sub>O<sub>55</sub> NMRs via strong adsorption. *RSC Adv* 6(10):8061–8069
  33. Epifani M, Arbiol J, Díaz R, Andreu T, Siciliano P, Morante JR (2010) Morphological and structural characterization of WO<sub>3</sub> and Cr–WO<sub>3</sub> thin films synthesized by sol–gel process. *Thin Solid Films* 518(16):4512–4514
  34. Martínez-de la Cruz A, Martínez DS, Cuéllar EL (2010) Synthesis and characterization of WO<sub>3</sub> nanoparticles prepared by the precipitation method: evaluation of photocatalytic activity under vis-irradiation. *Solid State Sci* 12(1):88–94
  35. Huang R, Shen Y, Zhao L, Yan M (2012) Effect of hydrothermal temperature on structure and photochromic properties of WO<sub>3</sub> powder. *Adv Powder Technol* 23(2):211–214
  36. Chiang TH, Hsu C-C, Chen T-M, Yu B-S (2015) Synthesis and structural characterization of tungsten oxide particles by the glycol method. *J Alloys Compd* 648:297–306
  37. Adhikari SP, Dean H, Hood ZD, Peng R, More KL, Ivanov I, Wu Z, Lachgar A (2015) Visible-light-driven Bi<sub>2</sub>O<sub>3</sub>/WO<sub>3</sub> composites with enhanced photocatalytic activity. *RSC Adv* 5(111):91094–91102
  38. Wang C, Zhang X, Yuan B, Wang Y, Sun P, Wang D, Wei Y, Liu Y (2014) Multi-heterojunction photocatalysts based on WO<sub>3</sub> nanorods: Structural design and optimization for enhanced photocatalytic activity under visible light. *Chem Eng J* 237:29–37
  39. Ahmed F, Kumar S, Arshi N, Anwar MS, Heun Koo B (2012) Morphological evolution between nanorods to nanosheets and room temperature ferromagnetism of Fe-doped ZnO nanostructures. *CrystEngComm* 14(11):4016–4026
  40. Ahmed Y, Yaakob Z, Akhtar P (2016) Correction: degradation and mineralization of methylene blue using a heterogeneous photo-Fenton catalyst under visible and solar light irradiation. *Catal Sci Tech* 6(4):1233–1233

41. Nidheesh PV (2015) Heterogeneous Fenton catalysts for the abatement of organic pollutants from aqueous solution: a review. *RSC Adv* 5(51):40552–40577
42. Yehia FZ, Eshaq G, Rabie AM, Mady AH, ElMetwally AE (2015) Phenol degradation by advanced Fenton process in combination with ultrasonic irradiation. *Egypt J Pet* 24(1):13–18
43. Ayodele OB, Lim JK, Hameed BH (2012) Degradation of phenol in photo-Fenton process by phosphoric acid modified kaolin supported ferric-oxalate catalyst: optimization and kinetic modeling. *Chem Eng J* 197:181–192
44. Segura Y, Molina R, Martínez F, Melero JA (2009) Integrated heterogeneous sono-photo Fenton processes for the degradation of phenolic aqueous solutions. *Ultrason Sonochem* 16(3):417–424
45. Zeng Z, Zou H, Li X, Arowo M, Sun B, Chen J, Chu G, Shao L (2013) Degradation of phenol by ozone in the presence of Fenton reagent in a rotating packed bed. *Chem Eng J* 229:404–411
46. Saleh R, Djaja NF (2014) UV light photocatalytic degradation of organic dyes with Fe-doped ZnO nanoparticles. *Superlattices Microstruct* 74:217–233
47. Yue C, Zhu X, Rigutto M, Hensen E (2015) Acid catalytic properties of reduced tungsten and niobium-tungsten oxides. *Appl Catal B* 163:370–381
48. Sayed Abhudhahir MH, Kandasamy J (2015) Synthesis and characterization of manganese doped tungsten oxide by microwave irradiation method. *Mater Sci Semicond Process* 40:695–700
49. Santhi K, Rani C, Dhilip Kumar R, Karuppachamy S (2015) Synthesis of nanoporous Zn-WO<sub>3</sub> by microwave irradiation method for photocatalytic applications. *J Mater Sci Mater Electron* 26(12):10068–10074
50. Beji N, Souli M, Ajili M, Azzaza S, Alleg S, Turki NK (2015) Effect of iron doping on structural, optical and electrical properties of sprayed In<sub>2</sub>O<sub>3</sub> thin films. *Superlattices Microstruct* 81:114–128
51. Silambarasan M, Saravanan S, Soga T (2015) Effect of Fe-doping on the structural, morphological and optical properties of ZnO nanoparticles synthesized by solution combustion process. *Phys E* 71:109–116
52. Husain S, Alkhtaby LA, Giorgetti E, Zoppi A, Muniz Miranda M (2016) Investigation of the role of iron doping on the structural, optical and photoluminescence properties of sol-gel derived TiO<sub>2</sub> nanoparticles. *J Lumin* 172:258–263
53. Siritwong C, Wetchakun N, Inceesungvorn B, Channei D, Samerjai T, Phanichphant S (2012) Doped-metal oxide nanoparticles for use as photocatalysts. *Prog Cryst Growth Charact Mater* 58(2–3):145–163
54. Steter JR, Rocha RS, Dionísio D, Lanza MRV, Motheo AJ (2014) Electrochemical oxidation route of methyl paraben on a boron-doped diamond anode. *Electrochim Acta* 117:127–133
55. Dobrin D, Magureanu M, Bradu C, Mandache NB, Ionita P, Parvulescu VI (2014) Degradation of methylparaben in water by corona plasma coupled with ozonation. *Environ Sci Pollut Res* 21(21):12190–12197
56. Sánchez-Martín J, Beltrán-Heredia J, Domínguez JR (2013) Advanced photochemical degradation of emerging pollutants: methylparaben. *Water Air Soil Pollut* 224(5):1483
57. Doná G, Dagostin JLA, Takashina TA, de Castilhos F, Igarashi-Mafra L (2018) A comparative approach of methylparaben photocatalytic degradation assisted by UV-C, UV-A and vis radiations. *Environ Technol* 39(10):1238–1249
58. Xiao X, Hu R, Tu S, Zheng C, Zhong H, Zuo X, Nan J (2015) One-pot synthesis of micro/nano structured  $\beta$ -Bi<sub>2</sub>O<sub>3</sub> with tunable morphology for highly efficient photocatalytic degradation of methylparaben under visible-light irradiation. *RSC Adv* 5(48):38373–38381
59. Kumar A, Shalini, Sharma G, Naushad M, Kumar A, Kalia S, Guo C, Mola GT (2017) Facile hetero-assembly of superparamagnetic Fe<sub>3</sub>O<sub>4</sub>/BiVO<sub>4</sub> stacked on biochar for solar photo-degradation of methyl paraben and pesticide removal from soil. *J Photochem Photobiol A* 337:118–131
60. Song H, Li Y, Lou Z, Xiao M, Hu L, Ye Z, Zhu L (2015) Synthesis of Fe-doped WO<sub>3</sub> nanostructures with high visible-light-driven photocatalytic activities. *Appl Catal B* 166–167:112–120
61. Zhang Z, haq M, Wen Z, Ye Z, Zhu L (2018) Ultrasensitive ppb-level NO<sub>2</sub> gas sensor based on WO<sub>3</sub> hollow nanosphers doped with Fe. *Appl Surf Sci* 434:891–897
62. Hernandez-Uresti DB, Sánchez-Martínez D, Martínez-de la Cruz A, Sepúlveda-Guzmán S, Torres-Martínez LM (2014) Characterization and photocatalytic properties of hexagonal and monoclinic WO<sub>3</sub> prepared *via* microwave-assisted hydrothermal synthesis. *Ceram Int* 40(3):4767–4775
63. Baserga A, Russo V, Di Fonzo F, Bailini A, Cattaneo D, Casari CS, Li Bassi A, Bottani CE (2007) Nanostructured tungsten oxide with controlled properties: synthesis and Raman characterization. *Thin Solid Films* 515(16):6465–6469
64. Yang C, Zhu Q, Lei T, Li H, Xie C (2014) The coupled effect of oxygen vacancies and Pt on the photoelectric response of tungsten trioxide films. *J Mater Chem C* 2(44):9467–9477
65. Yin L, Chen D, Feng M, Ge L, Yang D, Song Z, Fan B, Zhang R, Shao G (2015) Hierarchical Fe<sub>2</sub>O<sub>3</sub>@WO<sub>3</sub> nanostructures with ultrahigh specific surface areas: microwave-assisted synthesis and enhanced H<sub>2</sub>S-sensing performance. *RSC Adv* 5(1):328–337
66. Lin Y, Ferronato C, Deng N, Wu F, Chovelon J-M (2009) Photocatalytic degradation of methylparaben by TiO<sub>2</sub>: multivariable experimental design and mechanism. *Appl Catal B* 88(1–2):32–41
67. Yuan W, Zhang C, Wei H, Wang Q, Li K (2017) In situ synthesis and immobilization of a Cu(II)-pyridyl complex on silica microspheres as a novel Fenton-like catalyst for RhB degradation at near-neutral pH. *RSC Adv* 7(37):22825–22835
68. Kumar A, Sharma G, Naushad M, Kumar A, Kalia S, Guo C, Mola GT (2017) Facile hetero-assembly of superparamagnetic Fe<sub>3</sub>O<sub>4</sub>/BiVO<sub>4</sub> stacked on biochar for solar photo-degradation of methyl paraben and pesticide removal from soil. *J Photochem Photobiol A* 337:118–131
69. Ahmed Y, Yaakob Z, Akhtar P (2016) Degradation and mineralization of methylene blue using a heterogeneous photo-Fenton catalyst under visible and solar light irradiation. *Catal Sci Tech* 6(4):1222–1232
70. Anik M, Cansizoglu T (2006) Dissolution kinetics of WO<sub>3</sub> in acidic solutions. *J Appl Electrochem* 36(5):603–608
71. Velegraki T, Hapeshi E, Fatta-Kassinos D, Poullos I (2015) Solar-induced heterogeneous photocatalytic degradation of methylparaben. *Appl Catal B* 178:2–11